Real-time microscopic 3D shape measurement based on optimized pulse-width-modulation binary fringe projection

You may also be interested in:

Absolute three-dimensional micro surface profile measurement based on a Greenough-type stereomicroscope
Yan Hu, Qian Chen, Tianyang Tao et al.

Defocusing rectified multi-frequency patterns for high-precision 3D measurement
Hai-Qing Huang, Xiang-Zhong Fang and Wei Zhang

Simplified fringe order correction for absolute phase maps recovered with multiple-spatial-frequency fringe projections
Yi Ding, Kai Peng, Lei Lu et al.

Full-field phase error detection and compensation method for digital phase-shifting fringe projection profilometry
Chunwei Zhang, Hong Zhao, Lu Zhang et al.

3D shape measurement for moving scenes using an interlaced scanning colour camera
Senpeng Cao, Yiping Cao, Mingteng Lu et al.

Multiple spatial-frequency fringes selection for absolute phase recovery
Yi Ding, Jiangtao Xi, Yanguang Yu et al.

Measuring the 3D shape of high temperature objects using blue sinusoidal structured light
Xianling Zhao, Jiansheng Liu, Huayu Zhang et al.

Fringe-period selection for a multifrequency fringe-projection phase unwrapping method
Chunwei Zhang, Hong Zhao and Kejian Jiang

Real-time microscopic 3D shape measurement based on optimized pulse-width-modulation binary fringe projection

Yan Hu[1,2], **Qian Chen**[2], **Shijie Feng**[1,2], **Tianyang Tao**[1,2], **Hui Li**[1,2] **and Chao Zuo**[1,2,3]

[1] Smart Computational Imaging (SCI) Laboratory, Nanjing University of Science and Technology, Nanjing, Jiangsu Province 210094, People's Republic of China
[2] Jiangsu Key Laboratory of Spectral Imaging and Intelligent Sense, Nanjing University of Science and Technology, Nanjing, Jiangsu Province 210094, People's Republic of China

E-mail: huyanjackson@163.com and surpasszuo@163.com

Abstract

In recent years, tremendous progress has been made in 3D measurement techniques, contributing to the realization of faster and more accurate 3D measurement. As a representative of these techniques, fringe projection profilometry (FPP) has become a commonly used method for real-time 3D measurement, such as real-time quality control and online inspection. To date, most related research has been concerned with macroscopic 3D measurement, but microscopic 3D measurement, especially real-time microscopic 3D measurement, is rarely reported. However, microscopic 3D measurement plays an important role in 3D metrology and is indispensable in some applications in measuring micro scale objects like the accurate metrology of MEMS components of the final devices to ensure their proper performance. In this paper, we proposed a method which effectively combines optimized binary structured patterns with a number–theoretical phase unwrapping algorithm to realize real-time microscopic 3D measurement. A slight defocusing of our optimized binary patterns can considerably alleviate the measurement error based on four-step phase-shifting FPP, providing the binary patterns with a comparable performance to ideal sinusoidal patterns. The static measurement accuracy can reach 8 μm, and the experimental results of a vibrating earphone diaphragm reveal that our system can successfully realize real-time 3D measurement of 120 frames per second (FPS) with a measurement range of 8 mm $\times$ 6 mm in lateral and 8 mm in depth.

Keywords: phase measurement, three-dimensional sensing, binocular vision and stereopsis

S Supplementary material for this article is available online

(Some figures may appear in colour only in the online journal)

1. Introduction

In recent years, the mechanical testing of materials and structures commonly seen in MEMS has been an essential step towards the optimal design and reliability of micro-mechanical components. Dynamic 3D measurement is also of great importance in analyzing the behavior of micro-components, like the motion versus drive signal and shape changes during actuation. Fringe projection profilometry (FPP) is widely used in the 3D measurement of macro-scale objects due to its flexibility, noncontact nature and high accuracy [1]. The development of an electronic technique and electronic products, such as digital projectors and high speed cameras, have been pushing forward the improvement of 3D measurement speed

---

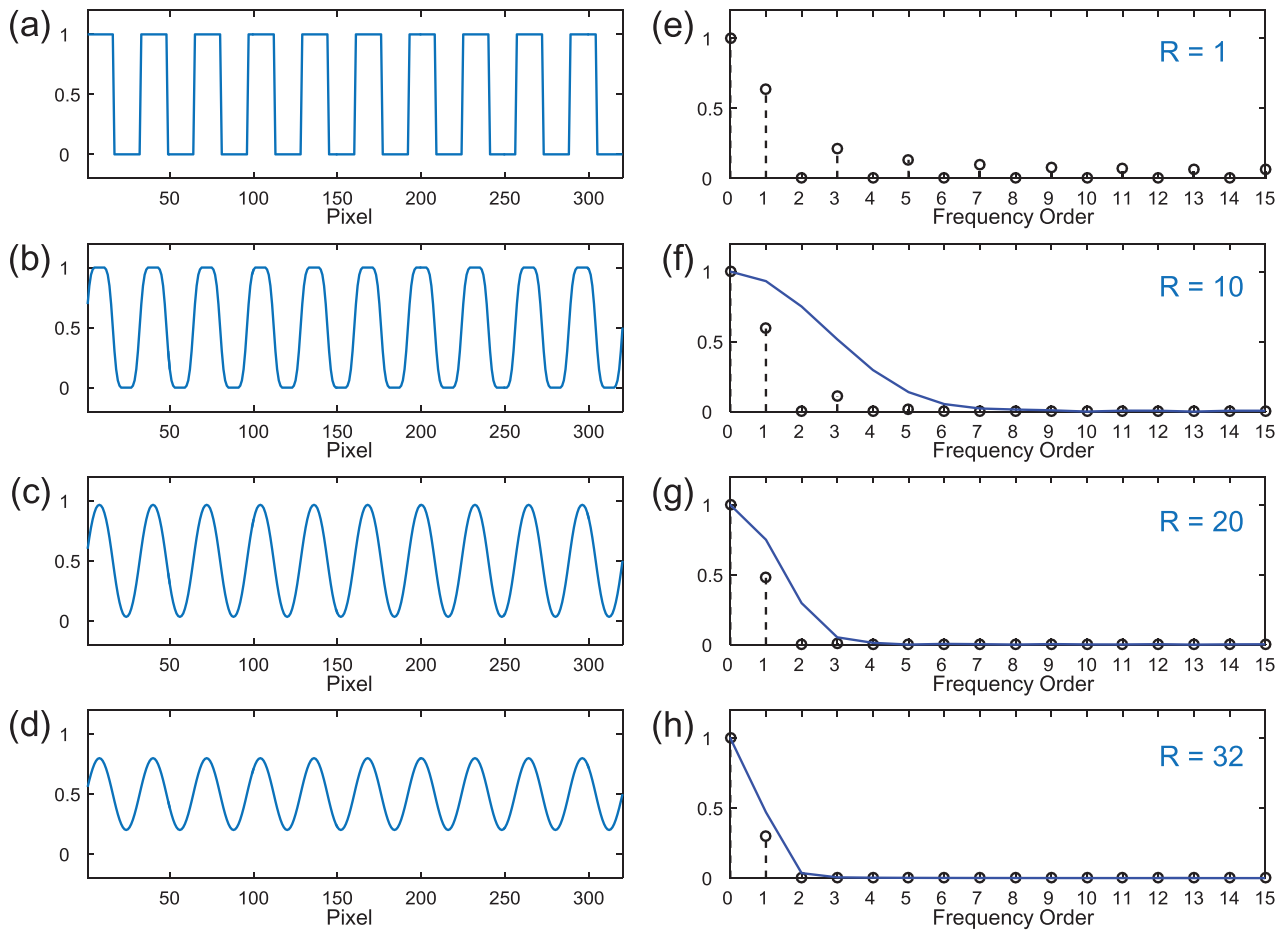[3] Author to whom any correspondence should be addressed.

Figure 1. An explanation of binary defocusing technology. (a) A binary squared waveform with a wavelength of 32 pixels; (b)–(d) fringe intensity cross profiles after defocusing of (a) corresponding to different sizes of filter kernel (10, 20 and 32 pixels); (e)–(h) the frequency components of (a)–(d). The blue curves in (f)–(h) represent the low-pass filter profiles and *R* is the radius of the 2D filter kernel.

and precision [2–6]. By combining the fringe projection setup with microscopic optics, the fringe pattern can be projected and imaged within a small area, making it possible to measure the 3D surfaces of micro-components [7–11]. Recently, some work on real-time microscopic FPP has also been reported [12, 13], in which the trade-off between accuracy and speed is still an intricate issue and deserves further investigation.

To realize real-time 3D measurements, the first important challenge we face is to improve the projection speed of the fringe patterns. Pixels on a digital micro-mirror device (DMD) only have two states, which means a DMD-based projector can only generate a binary pattern at a particular moment. Therefore, the multi-grey pattern can only be realized through time-domain integration of a series of one-bit pattern sequences with the length of each one-bit pattern in the time slot weighted by the corresponding power of 2 of its binary representation. One contradiction is that the multi-bit coded structured pattern realized by time integration goes against the fast projection procedure. To solve this problem, Lei and Zhang proposed a novel technique that uses binary structured patterns to realize 3D shape measurements based on binary defocusing [14]. Compared with another defocusing method proposed by Su *et al* [15] that uses a Ronchi grating, the digital binary fringe projection technique does not suffer from the phase-shift error and effectively avoids the gamma effect of the projector.

Binary fringe projection uses only '0's and '1's to construct patterns so that an ideal sinusoidal pattern cannot be directly produced. To improve the measurement accuracy, a binary defocusing technique is used to defocus the squared binary pattern into a sinusoidal fringe pattern. However, the contrast of the fringe will decrease a lot due to the defocusing. Ayubi *et al* presented methods for generating a binary pattern by sinusoidal pulse width modulation (SPWM) [16], which alleviates the effect of the binary pattern's high-order harmonics while keeping the fringe contrast at a reasonably high level. Based on this work, Wang and Zhang proposed optimal pulse width modulation (OPWM) [17]. However, the phase error caused by undesired high-order harmonics of the generated patterns based on SPWM and OPWM is still non-negligible, especially when the project is nearly in focus [18]. One effective way to eliminate the high-order harmonics side-effect is to use the phase-shifting algorithm with more phase-shifting steps [19]. By using a nine-step phase-shifting algorithm, Li and Zhang compared squared patterns against sinusoidal patterns in a microscopic application [13]. However, the utilized spatial phase unwrapping algorithm [12, 13] fails when the field of view contains discontinuous or spatially isolated surfaces.

The purpose of this paper is to design binary structured patterns that are suitable for dynamic micro-profile measurement. The patterns should have properties that facilitate fewer

Table 1. LUT to determine (k_h, k_l) according to round $[(15\phi_l - 7\phi_h)/2\pi]$ of the proposed two wavelengths.

Item	Content									
Round $[(15\phi_l - 7\phi_h)/2\pi]$	7	14	−1	6	13	−2	5	12	−3	4
k_h	1	2	2	3	4	4	5	6	6	7
k_l	0	0	1	1	1	2	2	2	3	3
Round $[(15\phi_l - 7\phi_h)/2\pi]$	11	−4	3	10	−5	2	9	−6	1	8
k_h	8	8	9	10	10	11	12	12	13	14
k_l	3	4	4	4	5	5	5	6	6	6

phase-shifting steps in order to suppress the non-sinusoidal effect of the binary patterns. SPWM and OPWM can generate better sinusoidal patterns because the unwanted harmonics in the spectrum are shifted to a higher frequency [19]. Thus, the unwanted harmonics become easier to suppress by defocusing. To further eliminate the side-effect of the high-order harmonics, we apply a four-step phase-shifting algorithm to calculate the phase value because it can only detect the odd orders of harmonics of the phase-shift images [20]. This property makes it possible to design binary patterns mainly composed of an even order of harmonics except the needed fundamental frequency. However, this is a difficult task because only two values are used to represent the structured patterns. Instead, we try to make the odd-order harmonics as little as possible, especially the 3rd, 5th, 7th, etc. Based on this idea, we design two binary patterns with different fringe wavelengths based on the optimization of SPWM. The patterns with a lower frequency (bigger wavelength) are utilized to help unwrap the phase value of the patterns with a higher frequency (smaller wavelength) based on the number–theoretical phase unwrapping approach [21]. Once the absolute phase value is obtained, the 3D information can then be derived after the system is calibrated [22]. Simulation is performed to show the effectiveness of our proposed method and real-time 3D reconstruction of a vibrating diaphragm of 120 frames per second is presented.

2. Principles

2.1. Defocusing technology of binary structured patterns

A sinusoidal pattern is flexible and easy to control, making it widely used in phase-shifting FPP. To improve the projection speed, binary squared patterns are used to replace the sinusoidal patterns in real-time measurement. However, a squared pattern is composed of more than one non-zero frequency component called high-order harmonics. To acquire a quasi-sinusoidal fringe, the squared binary pattern needs to be defocused. A simulation is presented here to show the effectiveness of binary defocusing. A Gaussian convolution is applied to simulate the defocusing with the kernel modeled as

$$g(x, y) = \frac{1}{2\pi\sigma^2} \exp\left(-\frac{x^2 + y^2}{2\sigma^2}\right). \quad (1)$$

Here, σ is the standard deviation of the filter kernel, which determines the degree of the defocusing. Figure 1 gives the 1D explanation of this progress. As the defocusing degree increases, the passband of the filter becomes narrower and the fringe becomes closer to ideal sinusoidal. The desired
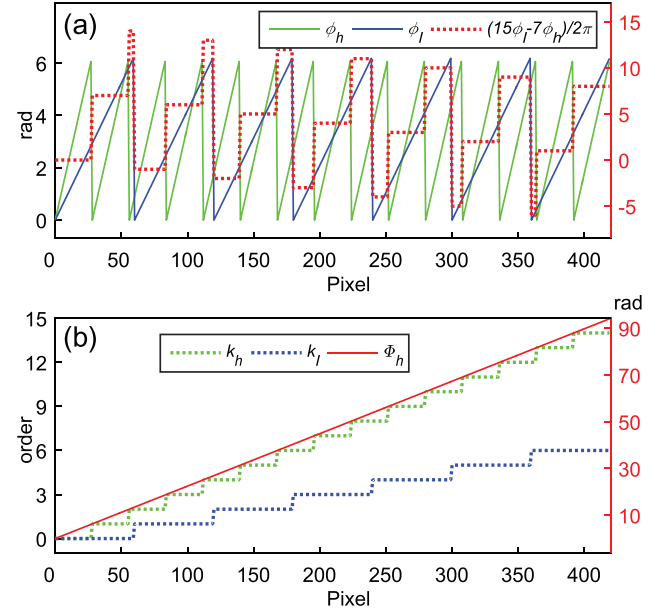

Figure 2. Illustration of the number–theoretical phase unwrapping approach using two patterns with different wavelengths (28 pixels and 60 pixels). (a) The relation of ϕ_h, ϕ_l, f_h and f_l; (b) the relation of k_h, k_l and Φ_h.

frequency component of an ideal sinusoidal pattern is up to the first order, so that a narrower passband corresponds to a waveform more sinusoidal. However, too much defocusing (figure 1(d)) leads to a drastic reduction of fringe contrast because the first order frequency is also suppressed considerably. To solve this problem, the binary pattern needs to be optimized to make it contain fewer high-order harmonics so that better fringe contrast can be realized because only a small degree of defocusing is needed. This part will be discussed in section 3.

2.2. Four-step phase-shifting algorithm

Phase-shifting methods have been widely used in optical metrology because of their high accuracy and flexibility. In phase-shifting FPP, a series of sinusoidal fringe patterns are projected to the test object surface using a digital projector, and the camera captures the reflected intensity from the test object surface. The captured intensity can be represented by

$$I_n(x, y) = I_a(x, y) + I_b(x, y) \cos[\phi(x, y)]. \quad (2)$$

Here, $I_n(x, y)$ is the intensity of the fringe pattern, $I_a(x, y)$ and $I_b(x, y)$ are the average intensity and the modulation of the fringe, respectively. ϕ represents the phase of the cosine function and is a key factor containing the 3D information
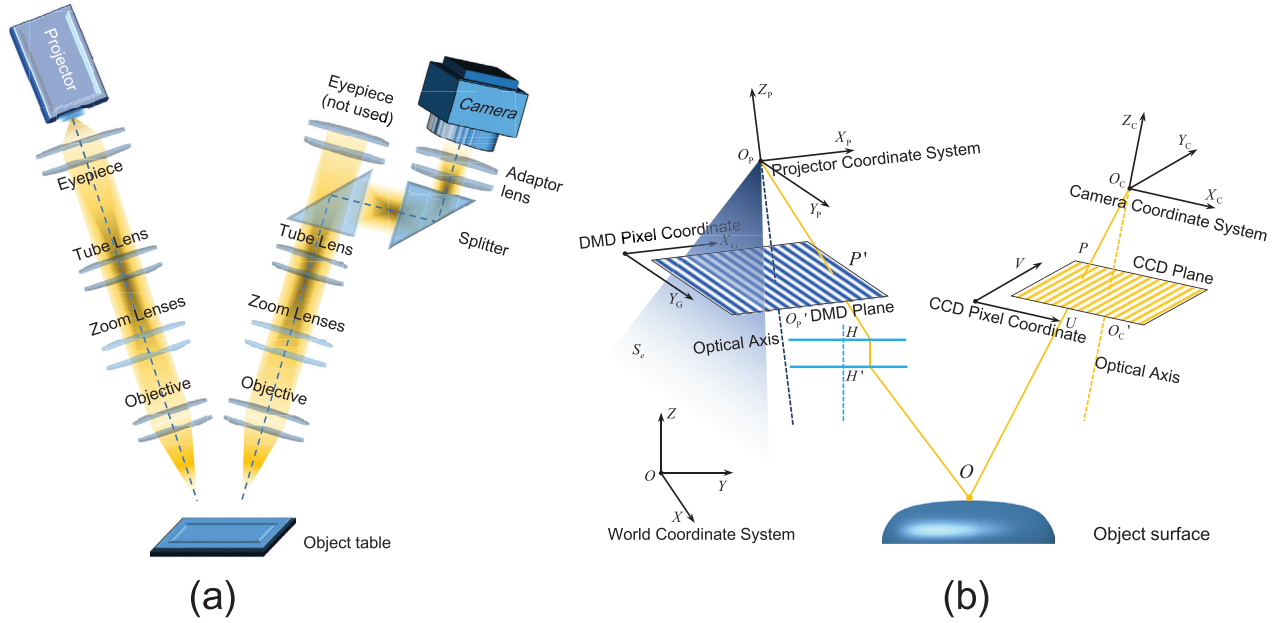
Figure 3. (a) The basic light path in our system setup; (b) the coordinate systems in our system setup.

of measured objects. (x, y) is the pixel coordinate of the camera. Many phase-shifting algorithms have been proposed [23] in recent decades. In general, they all have the ability-solving phase ϕ by several measured intensities. The minimum number of measurements required to reconstruct the unknowns in equation (2) is three, therefore a three-step phase-shifting algorithm is fairly acceptable. However, the three-step phase-shifting algorithm is very sensitive to non-sinusoidal components in the measured intensities. Instead, by using a four-step phase-shifting algorithm, the influence of all the even-order harmonics in the fringe can be automatically eliminated according to the characteristic polynomial P_z of the four-step phase-shifting algorithm [20]

$$P_z = 1 - z^2 + \mathrm{i}(z - z^3), \tag{3}$$

where $z = \exp(\mathrm{i}m\pi/2)$, m is the harmonics order. The zero points of the polynomial are ± 1 and i. The single root at $z = i$ allows the algorithm to detect the fundamental frequency and the root $z = \pm 1$ means that all the even-order harmonics ($m = \pm 2n, n$ is a non-zero integer) are harmless to the four-step phase-shifting algorithm. Based on this property, we can design suitable binary patterns which contain even-order harmonics as little as possible. The four fringe images with a phase shift of $\pi/2$ used in the four-step phase-shifting algorithm are

$$I_1(x, y) = I_a(x, y) + I_b(x, y) \cos[\phi(x, y)], \tag{4}$$

$$I_2(x, y) = I_a(x, y) + I_b(x, y) \cos[\phi(x, y) + \pi/2], \tag{5}$$

$$I_3(x, y) = I_a(x, y) + I_b(x, y) \cos[\phi(x, y) + \pi], \tag{6}$$

$$I_4(x, y) = I_a(x, y) + I_b(x, y) \cos[\phi(x, y) + 3\pi/2]. \tag{7}$$

Since the image number N is more than the number of unknowns, the least-squares algorithm is applied to solve the equations [23], and the wrapped phase value is given in the form of
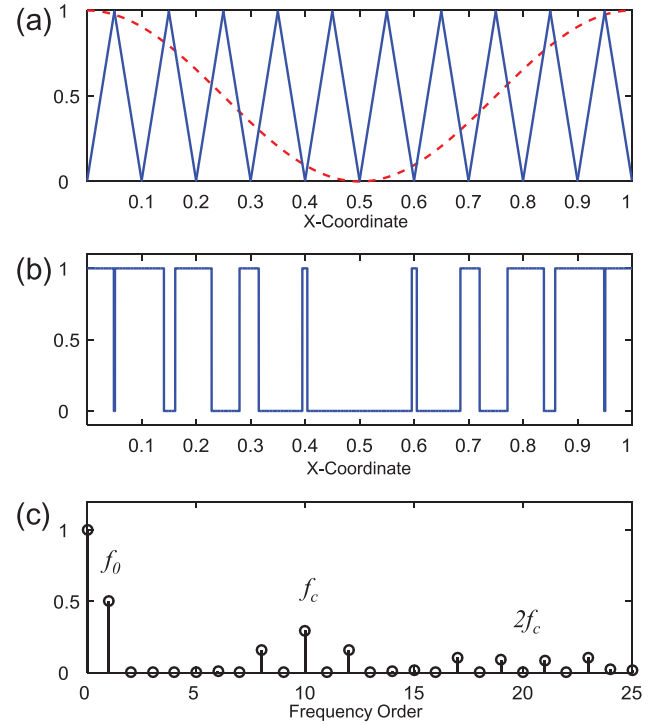

Figure 4. Basic idea of SPWM. (a) The sinusoidal and triangle waveform signals with $f_c = 10f_0$; (b) the generated binary SPWM waveform; (c) the spectrum of (b).

$$\phi = -\arctan \frac{\sum_{n=1}^{N} I_n \sin[2\pi(n-1)/N]}{\sum_{n=1}^{N} I_n \cos[2\pi(n-1)/N]}. \tag{8}$$

2.3. Absolute phase recovery

Equation (8) only provides the phase value wrapped in the range of $(0, 2\pi)$. In order to eliminate the ambiguity of phase
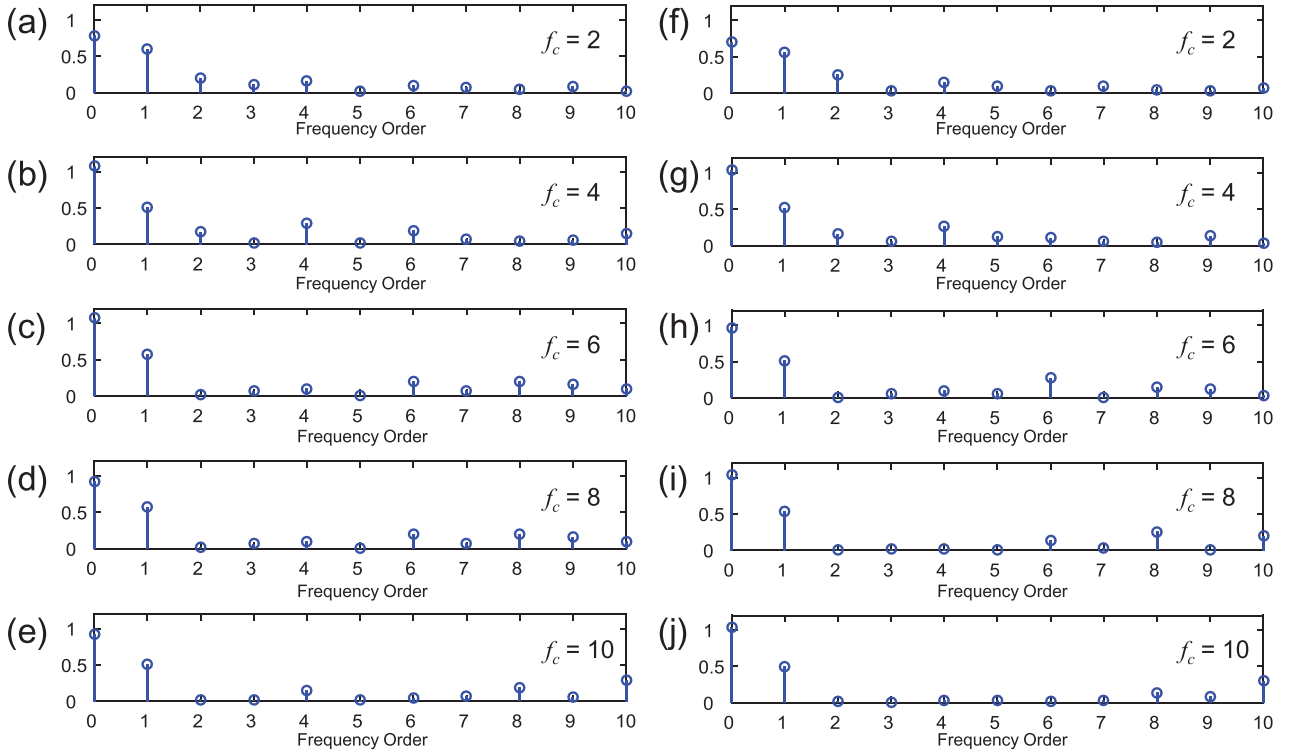
Figure 5. Spectrums of SPWM waveforms with the f_c/f_0 changing from 2 to 10; (a)–(e) the spectrums corresponding to the wavelength of 28 pixels; (f)–(j) the spectrums corresponding to the wavelength of 60 pixels.

Table 2. σ_p of the phase errors with the wavelength being 28 pixels.

Item	Content						
f_c	2	4	6	8	10	12	14
σ_p	0.083	0.029	0.056	0.055	0.030	0.084	0.358
f_c	16	18	20	22	24	26	28
σ_p	0.083	0.030	0.056	0.056	0.030	0.031	0.359

Table 3. σ_p of the phase errors with the wavelength being 60 pixels.

Item	Content						
f_c	2	4	6	8	10	12	14
σ_p	0.096	0.181	0.150	0.040	0.084	0.083	0.132
f_c	16	18	20	22	24	26	28
σ_p	0.131	0.084	0.084	0.041	0.149	0.160	0.095

orders, the wrapped phase value should be unwrapped to a continuous range by

$$\Phi(x, y) = \phi(x, y) + 2\pi k(x, y). \qquad (9)$$

Here, $\Phi(x, y)$ is the unwrapped phase value, and $k(x, y)$ is an integer that should be determined in each pixel. There are many proposed methods to do this work, which can be basically classified into two principle groups: spatial phase unwrapping and temporal phase unwrapping. Temporal phase unwrapping is an essential procedure to recover an unambiguous absolute phase even in the presence of large discontinuities or a spatially isolated surface [24].

We can get the wrapped phase value from equation (8) and the unwrapped phase value from equation (9) if $k(x, y)$ is obtained. In this work, the number–theoretical phase unwrapping approach [21, 25] is applied to realize the phase unwrapping. This method relies on the fact that, for a suitable chosen wavelength λ_l and λ_h, we can obtain a unique set of unwrapped phase values

$$\begin{cases} \Phi_l(x, y) = \phi_l(x, y) + 2\pi k_l(x, y) \\ \Phi_h(x, y) = \phi_h(x, y) + 2\pi k_h(x, y), \end{cases} \qquad (10)$$

where k_l and k_h are the fringe orders. The relation between Φ_l and Φ_h is expressed as $f_l \Phi_h = f_h \Phi_l$, where, f_l and f_h represent

the total number of the period of their corresponding patterns. The lowest common multiple (LCM) of λ_l and λ_h determines the maximum phase range that can be unwrapped. k_l and k_h can be derived through the relation:

$$(f_h \phi_l - f_l \phi_h)/2\pi = k_h f_l - k_l f_h. \qquad (11)$$

Generally, the value of equation (11) is an integer, so that the order pair (k_h, k_l) can be determined uniquely according to the value of the left side of equation (11). In this paper, f_h and f_l are chosen to be 15 and 7, respectively. When the measurement range is within the unambiguous measurement range LCM(λ_h, λ_l), a certain value of equation (11) can uniquely determine an order pair (k_h, k_l). These uniquely determined mapping relations are pre-stored in a look up table (LUT). After obtaining two wrapped phase values (ϕ_h, ϕ_l), we calculate their weighted difference $(f_h \phi_l - f_l \phi_h)/2\pi$ in equation (11). Then the calculated integer value of this result can be used to determine the fringe order pair (k_h, k_l) according to the LUT, as shown in table 1:

$$(k_h, k_l) = \text{LUT}\left[\text{round}\left(\frac{f_h \phi_l - f_l \phi_h}{2\pi}\right)\right]. \qquad (12)$$
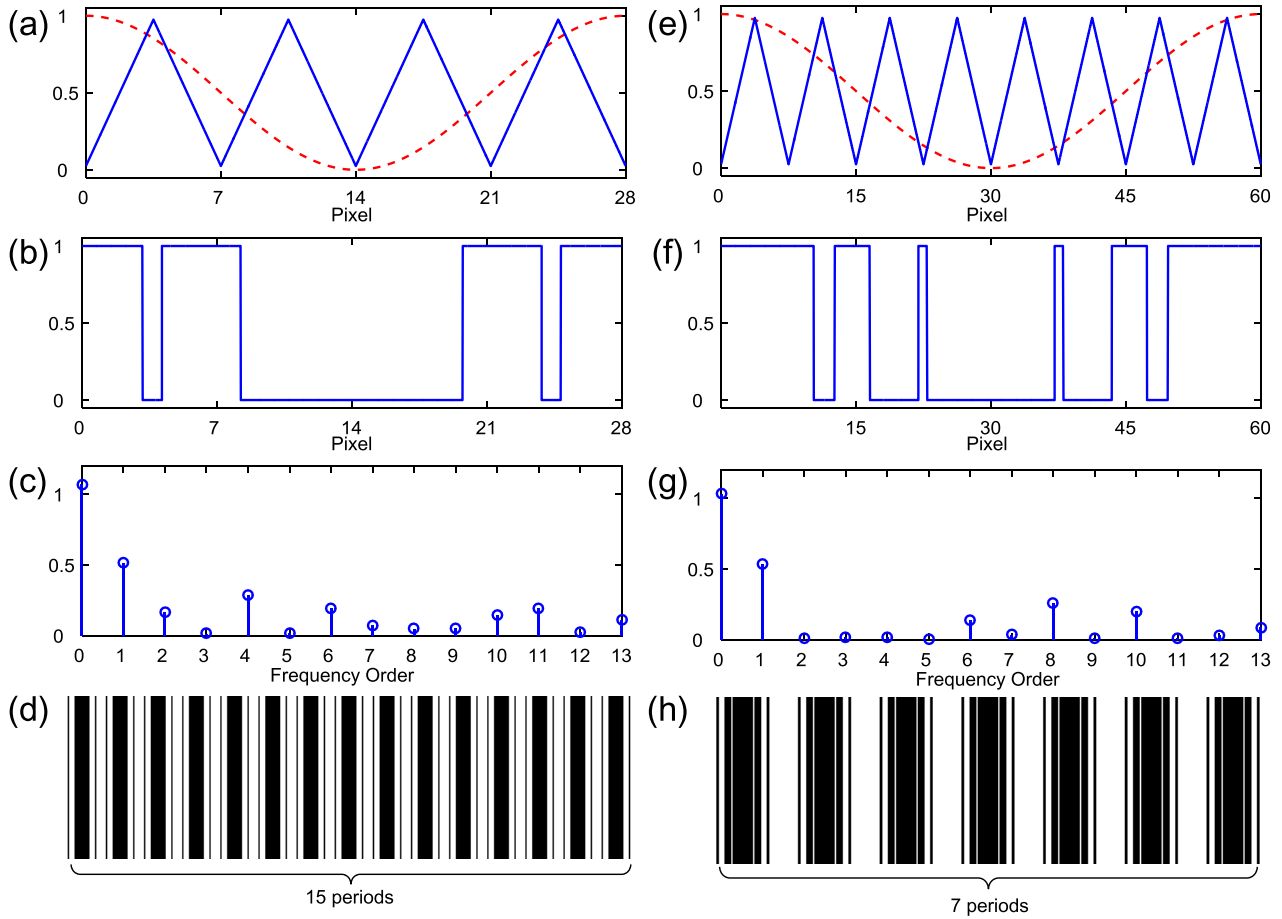
Figure 6. Information of the designed SPWM pattern with the wavelength being 28 pixels (left) and 60 pixels (right). (a) The sinusoidal and triangle waveforms with $f_c = 4f_0$; (b), (f) the generated binary SPWM waveform; (c), (g) the spectrums of (b) and (f), respectively; (d), (h) the 2D pattern based on (b) with 15 stripes and (f) with 7 stripes; (e) the sinusoidal and triangle waveforms with $f_c = 8f_0$.

Figure 2 is the illustration of the number–theoretical temporal phase unwrapping method used in our work ($\phi_h = 28$ pixels, $\phi_l = 60$ pixels, LCM(λ_h, λ_l) = 420 pixels). After obtaining the fringe order pair (k_h, k_l), the absolute phase value can be acquired through equation (10), as shown in figure 2(b). From equation (12), we can infer that $(f_h \phi_l - f_l \phi_h)/2\pi$ must be close to an integer so that the fringe order can be calculated correctly. Specifically, the maximum deviation of $(f_h \phi_l - f_l \phi_h)/2\pi$ should be less than 0.5. That is $|f_h \Delta \phi_l| + |f_l \Delta \phi_h| < \pi$. Suppose that the maximum value of both $\Delta \phi_l$ and $\Delta \phi_h$ is $\Delta \phi_{max}$, thus $(f_h + f_l)\Delta \phi_{max} < \pi$ should be satisfied. Combining the frequency value used in this paper, we can derive that $\Delta \phi_{max}$ should be less than 0.143 rad, which is fairly realizable.

2.4. Phase to height conversion

The change of the phase value in equation (2) is directly caused by the height distribution of the measured object. So when the absolute phase map is acquired, the depth information corresponding to each pixel of the camera can also be derived. Figure 3(a) gives the basic optical system in our setup. A Greenough-type stereomicroscope is used as the basic instrument in our system, which is composed of two totally separate coaxial optical paths. The projector is fixed upon the left eyepiece. The camera is fixed on the microscope

through a C-type adapter, which shares the light divided by a beam splitter in another tube of the microscope.

The corresponding coordinate system is shown in figure 3(b). $O - XYZ$ denotes the world coordinate system. UV is defined in the CCD plane, and $X_G Y_G$ is defined in the DMD plane. $O_P - X_P Y_P Z_P$ is the projector coordinate system, and $O_C - X_C Y_C Z_C$ is the camera coordinate system. $O_C O_C'$ and $O_P O_P'$ are the optical axes of the camera and the projector, respectively. H and H' refer to the principle points of the microscope parts, which includes the eyepiece, the tube lense, the zoom lense and the objective. According to our previous work [22], the relation between the depth z and the absolute phase Φ can be modeled as

$$z = \frac{\Phi m_1 + m_0}{n_1 \Phi + 1}, \qquad (13)$$

where, m_0, m_1 and n_1 are constant, which can be calculated through calibration.

3. Design of the binary structured patterns

3.1. Spectrum of SPWM waveforms

Binary defocusing technology enables squared binary structured patterns to replace ideal sinusoidal patterns in FPP [14].
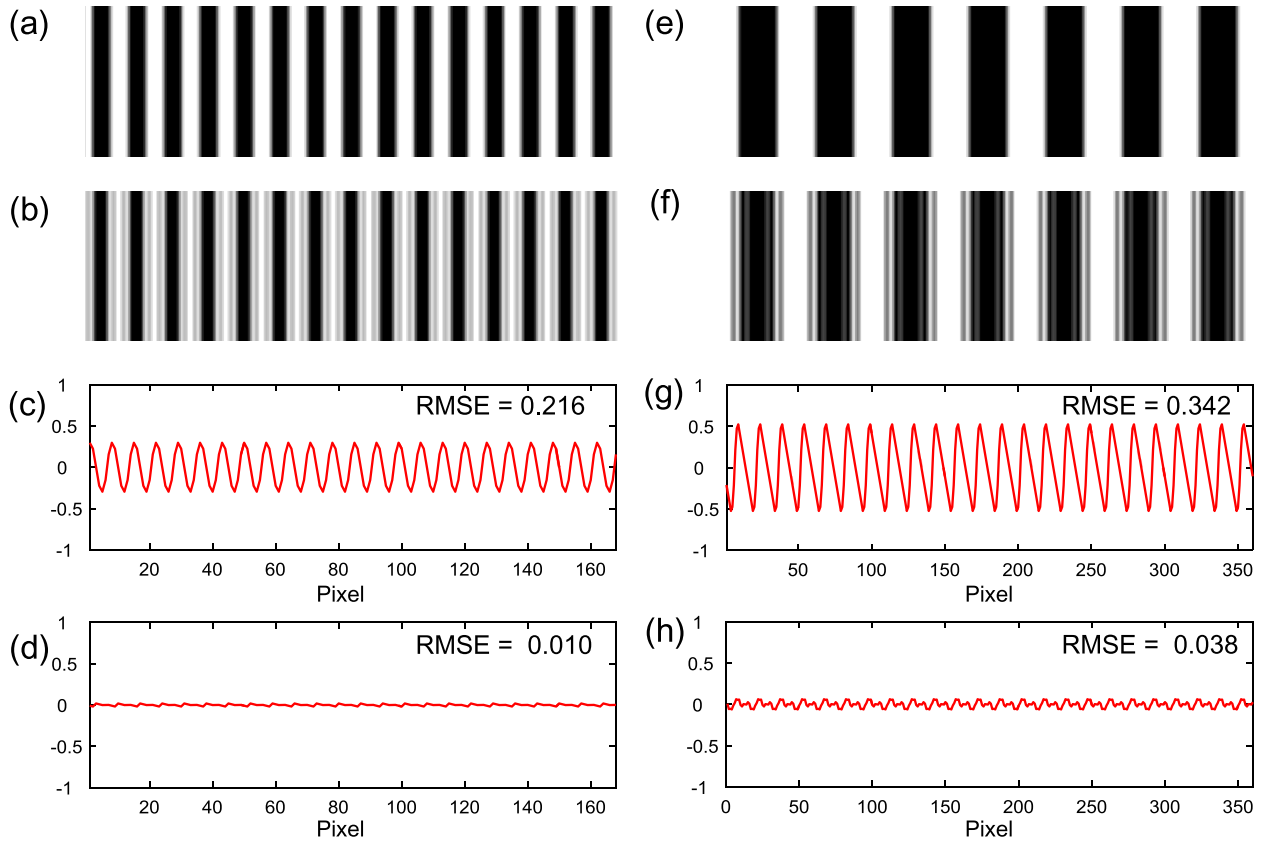
Figure 7. Comparison between the phase errors of the squared pattern and the designed SPWM pattern with the wavelength being 28 pixels (left) and 60 pixels (right). (a), (e) The defocused image of the squared patterns; (b), (f) the defocused image of the SPWM patterns; (c) the phase error using a squared pattern in (a) with RMSE = 0.216; (d) the phase error using an SPWM pattern in (b) with RMSE = 0.010; (g) the phase error using a squared pattern in (e) with RMSE = 0.342; (h) the phase error using an SPWM pattern in (f) with RMSE = 0.057.

However, when the squared binary pattern is only slightly defocused, more phase-shifting steps are needed to suppress high-order harmonics. To acquire a high quality sinusoidal pattern through a small defocusing level, the SPWM technique is introduced to generate binary patterns [16]. An SPWM waveform is modulated by comparing an ideal sinusoidal waveform with a high frequency triangular carrier. Figure 4(a) shows the basic idea of SPWM. The areas where the sinusoidal pattern has greater value than the triangular carrier are set as '1', and the rest of the modulated binary pattern is '0'. Assume that the fundamental frequency of the sinusoidal signal is f_0 and the carrier frequency of the triangle $f_c = 10f_0$; figure 4(b) gives the SPWM waveform composed of '0's and '1's. Ideally, as shown in figure 4(c), the higher frequency components are shifted farther away from the fundamental frequency so that the harmonic orders of the SPWM waveform become

$$N_{SPWM} = nf_c \pm kf_0. \tag{14}$$

When n is an odd integer, k is even, and when n is an even integer, k is odd. SPWM performs well when the signal is spatially continuous. However, the discrete nature of the digital projection device limits the design of ideal SPWM patterns. In particular, when the fringe period is narrow, the spectrum of the SPWM waveform will no longer be like equation (14).

Apart from the ambient noise, the measurement error in phase-shifting FPP mainly comes from the harmonics in the non-sinusoidal pattern. Improving the phase-shifting step contributes to the suppression of more harmonics, but this would hinder measurement speed due to the involvement of additional patterns. Although SPWM or OPWM makes the binary pattern closer to a sinusoidal one, the spectrum still contains the side bands of the carrier frequency f_c, which cannot be neglected. If f_c/f_0 is an even integer, the predominant high-order harmonics around f_c of the SPWM waveform are even orders which will not cause any errors when the four-step phase-shift algorithm is applied. Although harmonics on the side of $2f_c$ and some higher order of harmonics may be odd, they almost have no impact because they can be easily filtered, even in a nearly focused system. Zuo *et al* showed some optimized SPWM patterns applied in the measurements of macro-objects [19]. In our microscopic 3D shape measurement system, the properties of the stereomicroscope are considered since the depth of field and the field of view of a microscope are both quite small compared to a traditional optical system. Combining these properties, we design two sets of binary patterns with different periods to realize phase unwrapping using the number–theoretical algorithm.

3.2. Designing principles

When designing SPWM waveforms, several key issues should be considered. Firstly, denser fringe patterns require fewer pixels in one fringe period. However, the number of pixels in
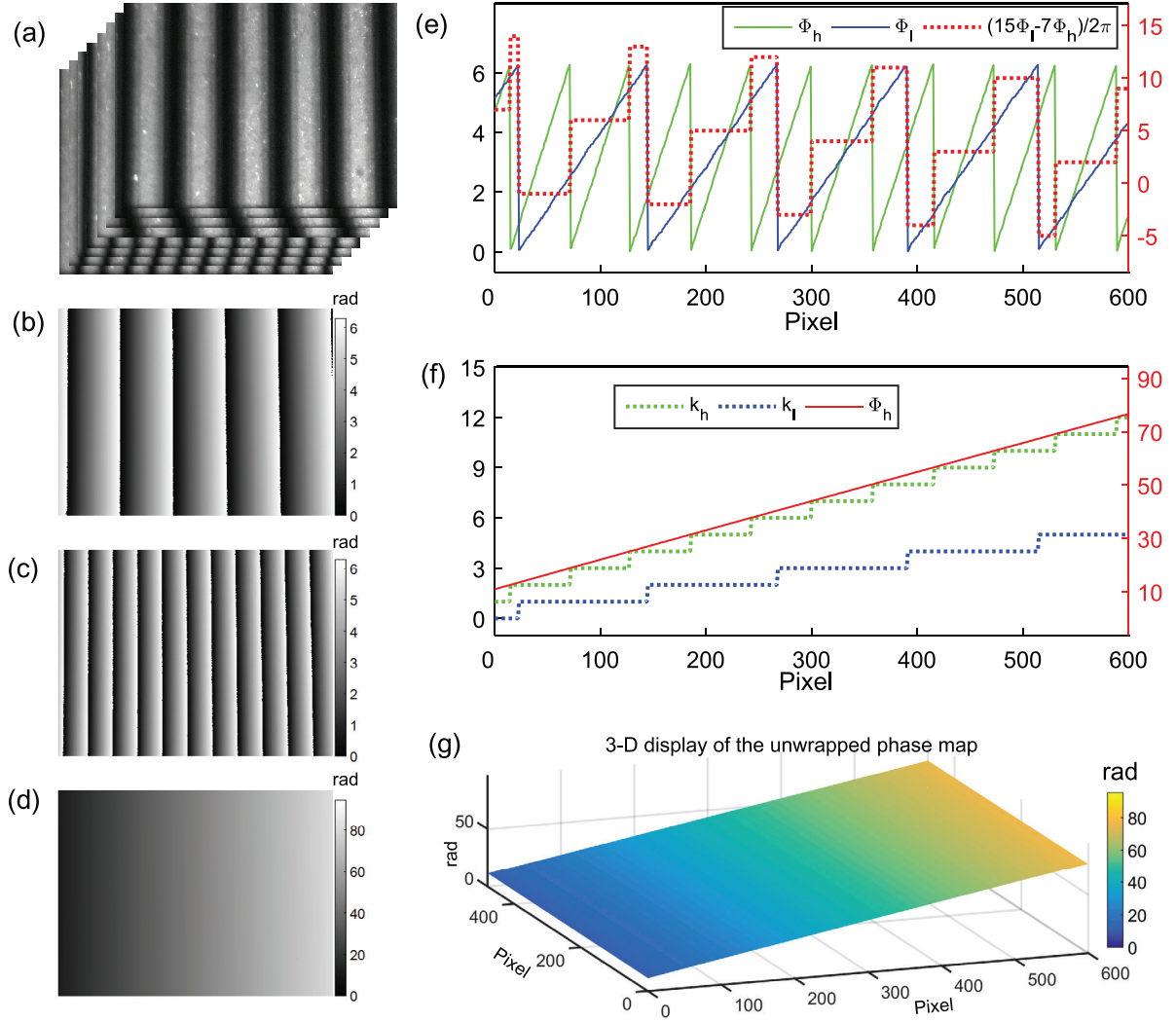
Figure 8. Phase unwrapping test of a plate. (a) The captured images; (b), (c) the wrapped phase solved by equation (8) respectively based on the patterns with a wavelength of 60 pixels and 28 pixels; (d) the unwrapped phase map with its 3D image shown in (g); (e), (f) the detailed information of the 100th line of the phase map.

one period should be a multiple of four to allow an accurate four-step phase shift. Secondly, the carrier frequency f_c cannot be infinitely large due to the discrete nature of the DMD. Therefore, we cannot directly acquire an ideal SPWM waveform. Instead, we generate a nearly ideal SPWM waveform using a high sample rate (1000), and then extract the discrete, equally spaced pixels to make up a fringe pitch that can be loaded on the DMD. After the wavelength of the fringe is confirmed, we optimize the carrier frequency by changing f_c incrementally from twice over f_0 until the spectrum fits the requirement as displayed in figure 4(c). Figure 5 gives two groups of spectrums of SPWM waveforms with the f_c/f_0 changed from 2 to 10. The left column corresponds to the fringe period of 28 pixels, and the right column corresponds to the fringe period of 60 pixels. We can intuitively speculate the fringe quality by checking the value of the unwanted harmonics. Nevertheless when their distributions are similar, it is difficult to distinguish the ideal one. To explain how to choose the best f_c from the candidates, a simulation of calculating phase errors using these candidates is carried out. The first simulated wavelength is 28 pixels. The defocusing is simulated using a Gaussian filter with a 6×6

square and the standard deviation σ of two. The measurement noise is simulated with a normal distribution $N(0, 0.01^2)$. Table 2 gives the result of the simulation with the root-mean-square error (RMSE) σ_p corresponding to different f_c. The same process is also conducted with the wavelength of 60 pixels, and the result is listed in table 3. The RMSE σ_p of each result is averaged by five simulation results. According to tables 2 and 3, we can choose f_c with the minimum σ_p.

Following this strategy, we generate two optimized SPWM waveforms with their wavelengths being 28 and 60 pixels, respectively. Figure 6 is the corresponding information of the generated fringe patterns. It should be noted that the LCM of (28, 60) is 420, which is less than the column number of the DMD (608). We move the used 420 columns of the digital patterns into the centre of the DMD to make sure the camera can capture the fringes easily.

3.3. Simulations

To show the performance of the designed patterns, simulations are carried out to compare the designed patterns with
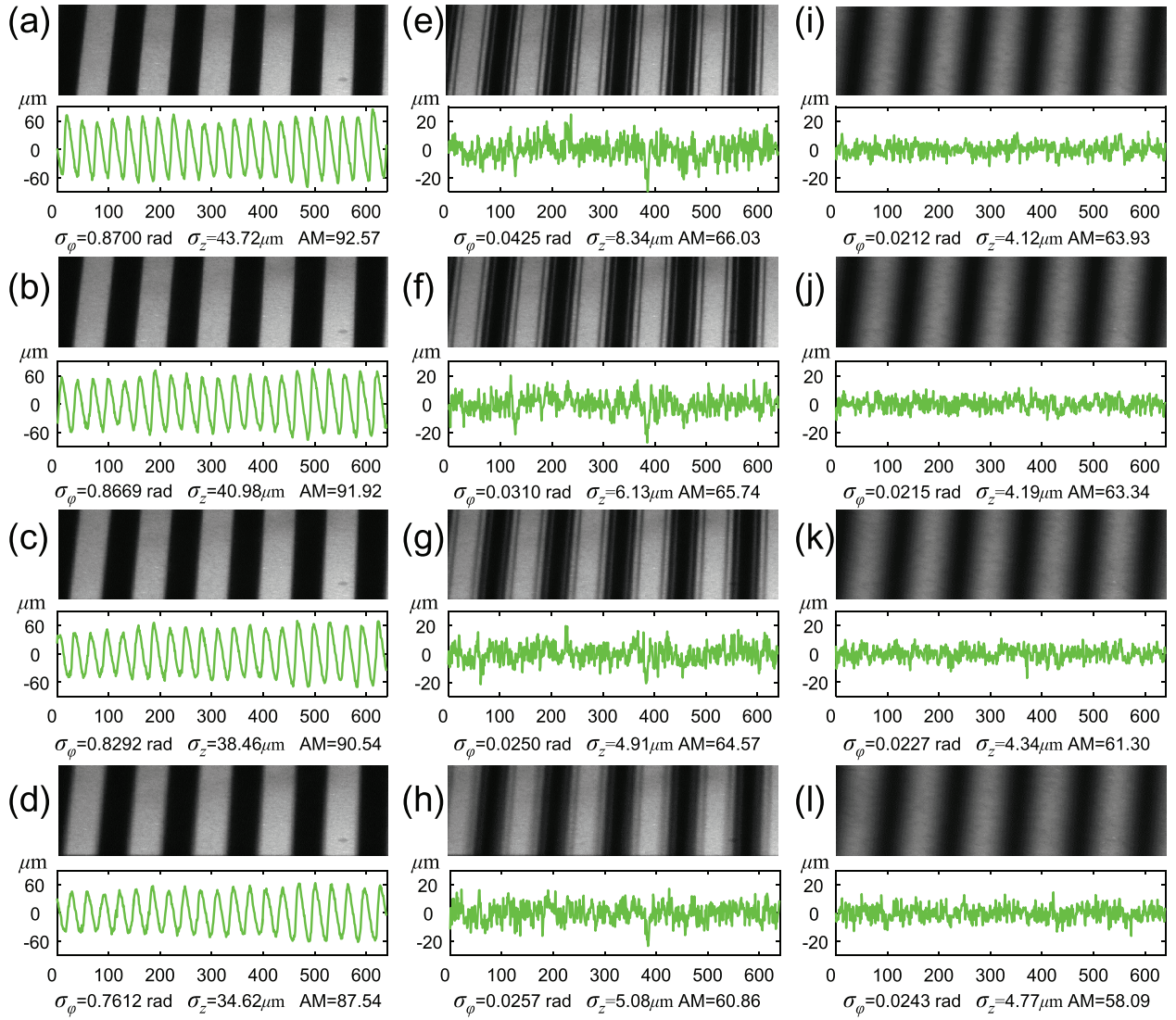
Figure 9. Static measurement results of a ceramic substrate using squared patterns, proposed SPWM patterns and sinusoidal patterns with a four-step phase-shifting algorithm. (a)–(d) The measurement results corresponding to the squared patterns with an increase in the defocusing level; (e)–(h) the measurement results corresponding to the optimized SPWM patterns with an increase in the defocusing level; (i)–(l) the measurement results corresponding to the sinusoidal patterns with an increase in the defocusing level.

the squared binary patterns. Noise is not considered in the simulations for a direct comparison between the performance of the different patterns. The proposed SPWM patterns with 28 pixels and 60 pixels are labeled with p_h and p_l, respectively. The squared patterns with 28 pixels and 60 pixels are labeled with s_h and s_l, respectively. The defocusing is simulated by a Gaussian filter with a 5×5 square and a standard deviation of 5/3. The four-step phase-shift algorithm is applied to p_h, s_h, p_l and s_l. The phase error using s_h (figure 7(a)) is shown in figure 7(c) with an RMSE of 0.216 rad, which is nearly 20 times that of the error using p_h (figure 7(b)), as shown in figure 7(d). The phase error using s_l (figure 7(e)) is shown in figure 7(g) with an RMSE of 0.342 rad, which is also much bigger than the error using p_l (figure 7(f)), as shown in figure 7(h).

The simulation result reveals that the phase error of the proposed pattern drastically reduces compared with the squared pattern at the same defocusing level, which shows

the potential of our proposed method for combining the four-step phase-shifting algorithm with the optimized SPWM pattern. Besides, it can be seen from figures 7(d) and (h) that the phase error is always less than $0.1(<0.143)$ rad. Based on the analysis at the end of section 2.3, the chosen fringe patterns will not suffer from the problem of fringe order error in the unwrapping process.

4. Experiments

To testify the performance of our proposed method, experiments were conducted using a system composed of a stereo-microscope (with a magnification adjustable from $0.8\times$ to $5\times$), a digital projector (a LightCrafter based on a DLP3000 DMD chip with a resolution of 684×608) and a digital camera (Basler acA640–750 um with a resolution of 640×480 and a max frame rate of 751 FPS).
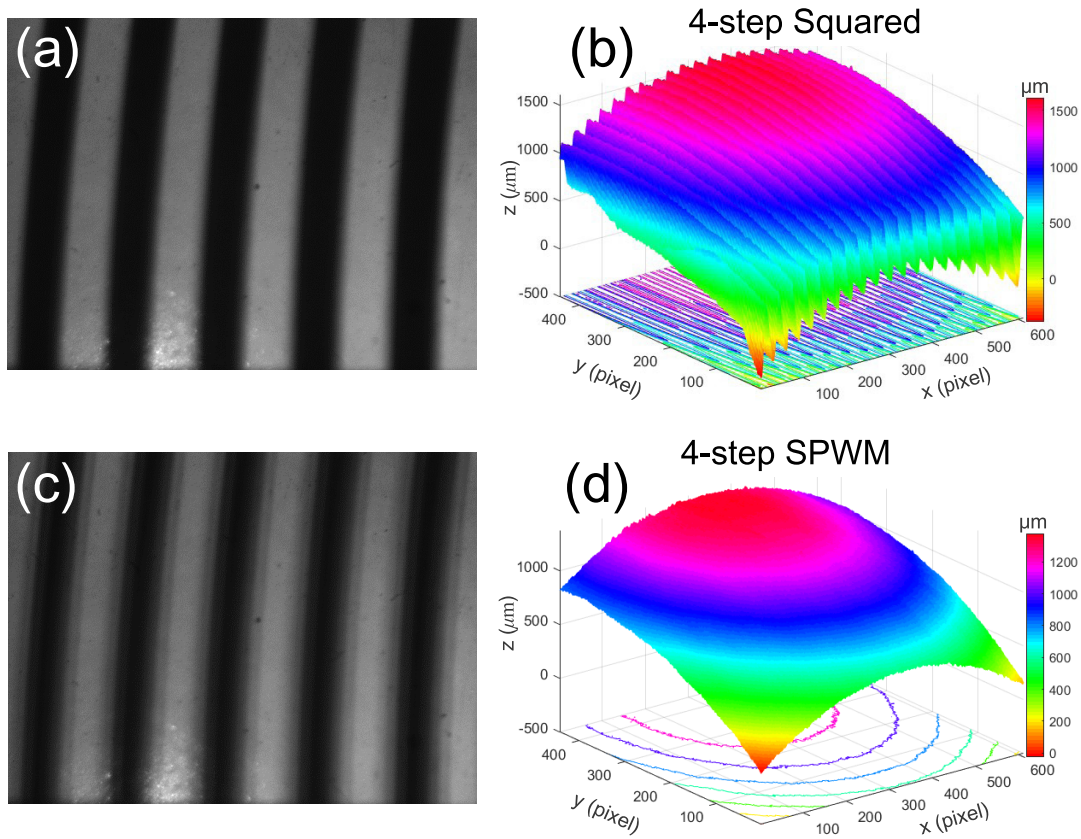
Figure 10. Static measurement results of an earphone diaphragm using squared patterns and the proposed SPWM patterns with the four-step phase-shifting algorithm. (a) A captured image using squared patterns; (b) the 3D reconstruction of the diaphragm using the four-step phase-shifting algorithm based on squared patterns; (c) a captured image using SPWM patterns; (d) the 3D reconstruction of the diaphragm using the four-step phase-shifting algorithm based on SPWM patterns.
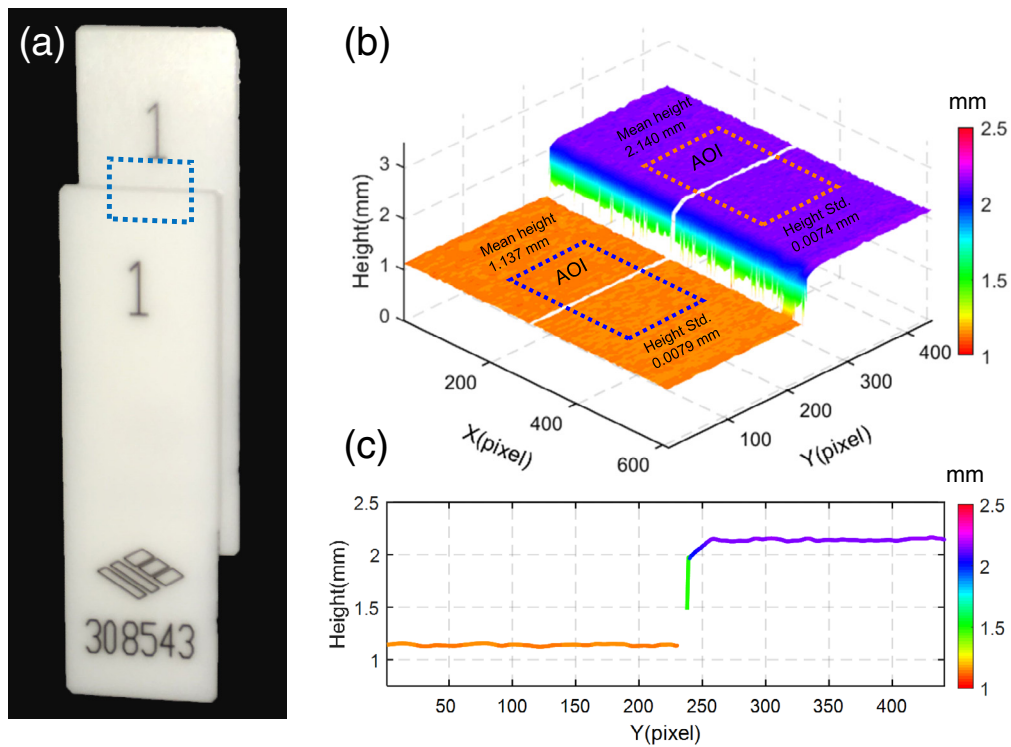

Figure 11. Static measurement results of a step structure composed of two ceramic blocks. (a) The measured sample with the reconstructed area marked in a blue rectangle; (b) the 3D reconstruction of the blue rectangle area in (a); (c) the cross section of the white line in (b).
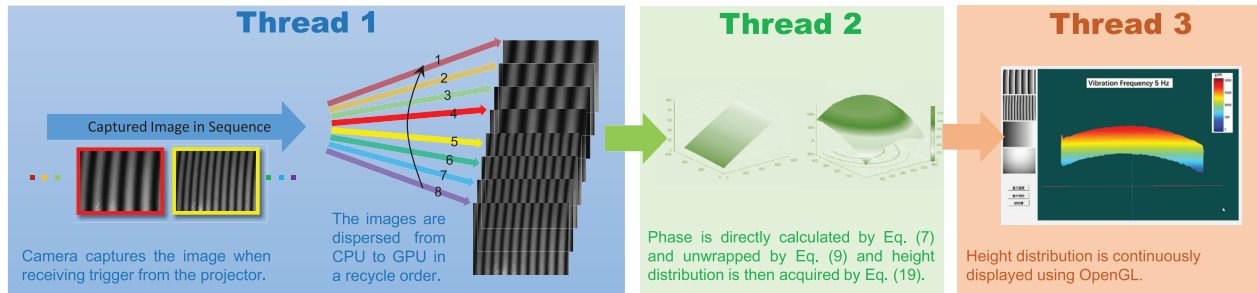
Figure 12. Framework of our programmed software. Thread 1 is for the image storage; thread 2 is for data processing; thread 3 is for real-time 3D display.
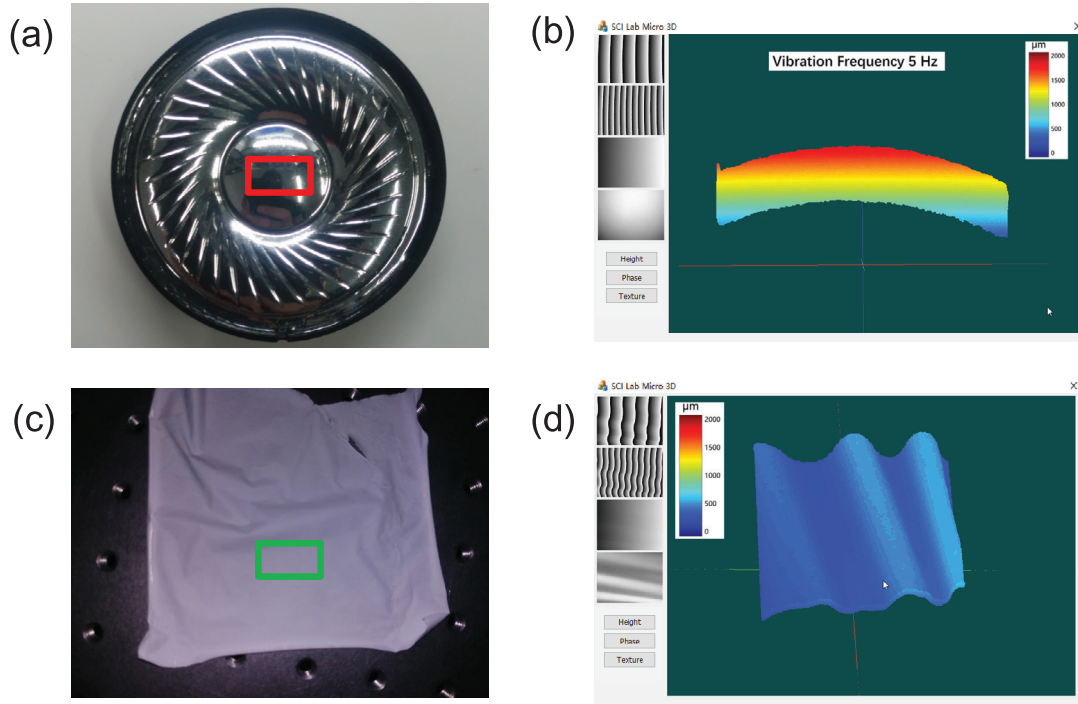

Figure 13. Real-time measurement of a vibrating earphone diaphragm and a rubber diaphragm. (a), (c) the measured objects; (b) one reconstructed frame of the area in the red rectangle of (a); (d) one reconstructed frame of the area in the green rectangle in (c).

4.1. Phase unwrapping

Firstly, a plate was measured to confirm the feasibility of the phase unwrapping using our proposed binary patterns. Figure 8(a) shows the captured images. Figures 8(b) and (c) show the wrapped phase of the two sets of the fringe. Figure 8(d) shows the unwrapped phase map with its 3D image shown in figure 8(g). Figures 8(e) and (f) are the detailed information of the 100th line of the phase map. This result clearly proves that the proposed phase unwrapping scheme is practicable in experiments.

4.2. Defocusing analysis

Combined with the four-step phase-shifting algorithm, four different levels of defocusing were performed to measure a ceramic substrate using squared patterns, proposed SPWM patterns and sinusoidal patterns, respectively. The measurement accuracy is represented by σ_ϕ and σ_z, which refer to the RMSE of the measured phase and depth, respectively.

The average modulation (AM) of each fringe is also calculated as a reference.

Figures 9(a)–(d) are the images (up) and height distribution of the 100th row (down) corresponding to the squared patterns with an increase in the defocusing level. Figures 9(e)–(h) are the images (up) and height distribution of the 100th row (down) corresponding to the optimized SPWM patterns with an increase in the defocusing level. Figures 9(i)–(l) are the images (up) and height distribution of the 100th row (down) corresponding to the sinusoidal patterns with an increase in the defocusing level. σ_ϕ and σ_z of the 100th row is attached below the image as well as the AM. The primary impression of the result is that the accuracy using our optimized SPWM patterns is much better than that of the squared patterns, which is very consistent with the simulation result in figure 7. We can also find that as the defocusing level increases, the phase error of the squared patterns reduces little. However, the phase error using the optimized SPWM patterns decreases obviously from 0.0425 to 0.0257. The AM of the SPWM patterns is always bigger than that of the sinusoidal patterns.
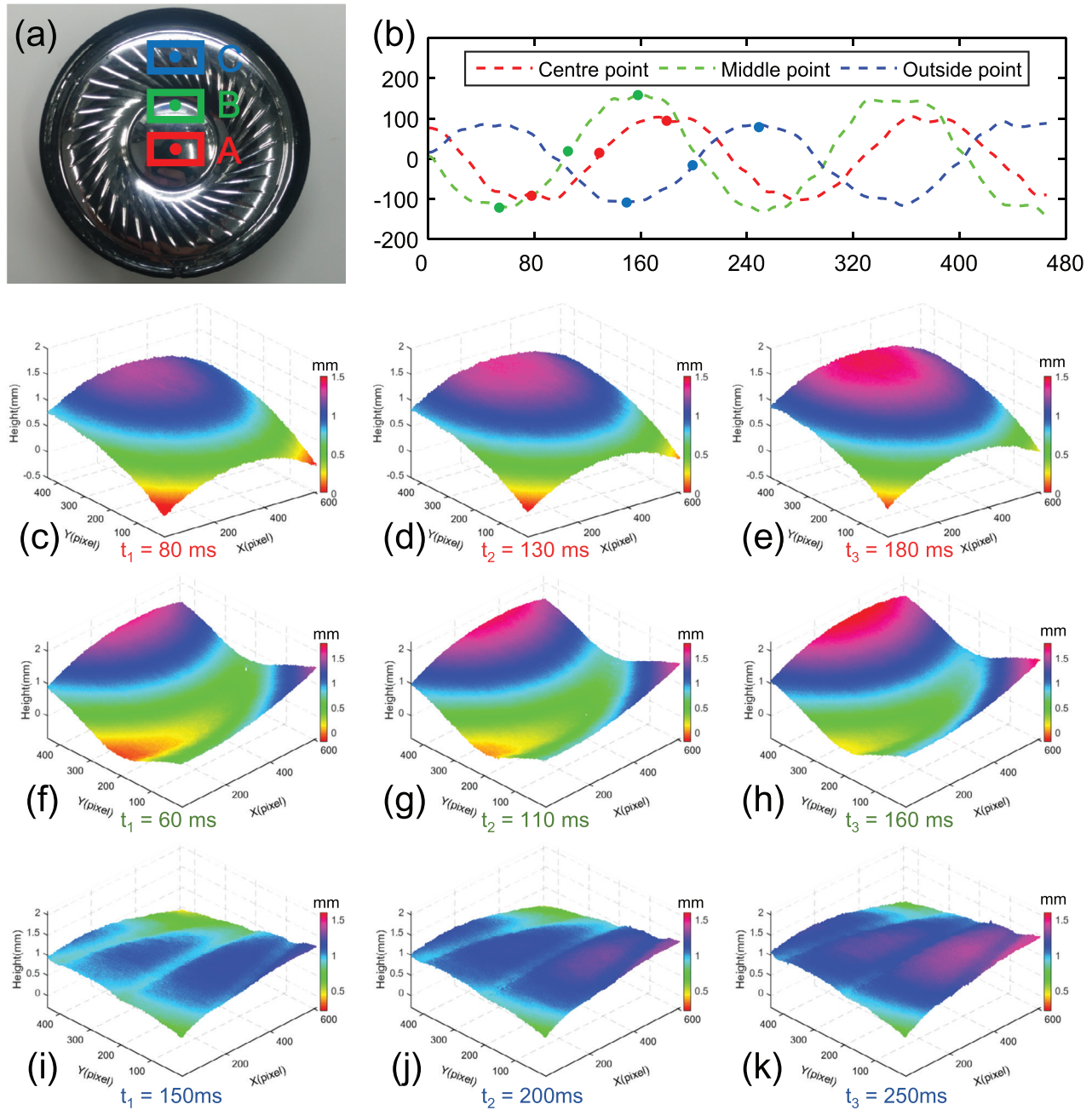
Figure 14. Vibrational states of three different areas of the earphone diaphragm vibrating at 5 Hz. (a) The object marked with measured areas and points; (b) the vibration curves of three points marked in (a); (c)–(e) three height maps of three moments (80 ms, 130 ms and 180 ms) corresponding to the red marked area A; (f)–(h) three height maps of three moments (60 ms, 110 ms and 160 ms) corresponding to the green marked area B; (i)–(k) three height maps of three moments (150 ms, 120 ms and 250 ms) corresponding to the blue marked area C.

This phenomenon can be explained by figures 6(c) and (g), which prove that the fundamental frequency component of both designed SPWM patterns are above 0.5. In conclusion, when a slight defocusing is involved, the performance of our designed optimized binary SPWM patterns compares favourably with the sinusoidal patterns. However, only 1 bit is used to represent the proposed patterns.

4.3. Static measurements

To further testify the performance of the proposed combination of the four-step phase-shifting algorithm with our proposed patterns, we conducted two static measurements of an earphone diaphragm and a sample composed of two calibrated artifacts.

In the first experiment, the four-step phase-shifting algorithm is applied to both our optimized patterns and the squared patterns. The measurement result is shown in figure 10. The 3D reconstruction of figures 10(a) and (c) are labeled with the contour line under the shape as shown in figures 10(b) and (d), respectively. This result clearly shows the effectiveness of our proposed method in harmonics elimination.

Another experiment is then conducted to quantitatively show the measurement accuracy of our system, as shown in figure 11. The measured object is a step structure composed of two standard ceramic blocks, which are 1 mm thick with a
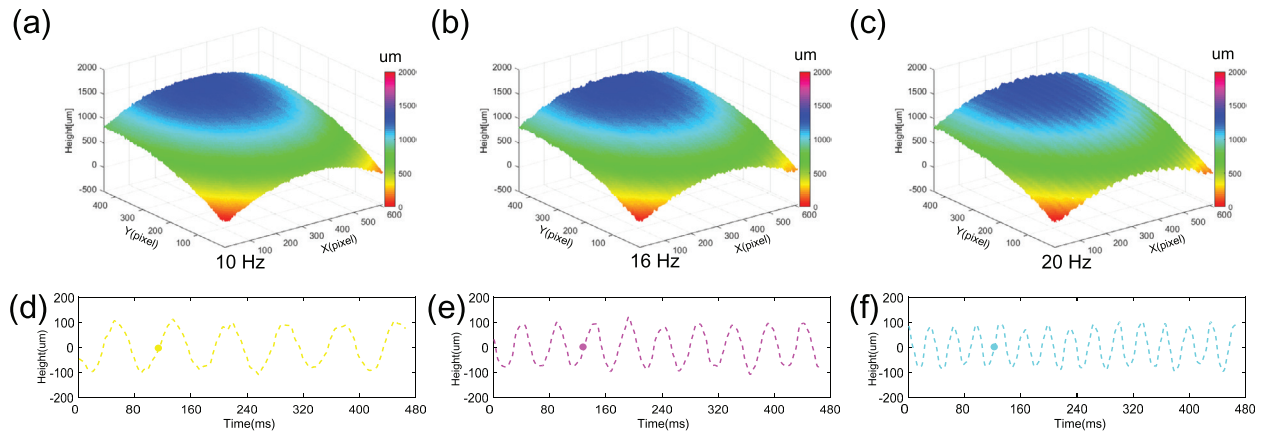
Figure 15. Vibrational states of the central area of the earphone diaphragm in different frequencies. (a) 3D map in the moment marked with a point in (d); (b) 3D map in the moment marked with a point in (e); (c) 3D map in the moment marked with a point in (f); (d)–(f) the vibrational curves of the red point marked in figure 14 (a) at 10 Hz, 16 Hz and 20 Hz, respectively.

precision of 1.34 μm provided by the manufacturer. The 3D reconstruction of the area in the blue rectangle in figure 11(a) is shown in figure 11(b). The higher surface has a mean height value of 2.140 mm with a standard deviation of 0.0074 mm and the lower surface has a mean height value of 1.137 mm with a standard deviation of 0.0079 mm. The cross section of the white line in figure 11(b) is provided in figure 11(c) with the height value color coded. The disconnection in the line is because the steep side of the step cannot be correctly imaged.

4.4. Dynamic measurements

To show the real-time measurement potential of our system setup, we programme a C++-based GUI to dynamically show the 3D result of objects. GPU acceleration and multi-threading programming technology are implemented to display the 3D result in real-time. The projection speed is set at 400 Hz. The reconstruction speed can reach 120 FPS. The main framework of the data processing is shown in figure 12. The projector projects each binary pattern and sends the trigger signal to the camera, and then the camera transports the image into the CPU. The captured image is then dispersed into GPU RAM, which allocates eight constant memory spaces for temporary storage of the images. In thread 2, the processing of these images is accomplished. Once a height distribution is calculated, it will start another calculation no matter whether new images are updated or not. The third thread also works separately and refreshes the 3D display of the height distribution at a constant rate, e.g. 120 FPS.

Dynamic measurements were conducted on a moving-coil earphone and a rubber diaphragm, as shown in figure 13. The earphone diaphragm vibrates at 5 Hz, which is driven by a self-designed high speed D/A converter. Figure 13(a) is the measured diaphragm and figure 13(b) is one frame reconstructed. Another measured object is a rubber diaphragm (figure 13(c)) which is pulled tight with structural undulation, as shown in figure 13(d). Both measurement results are recorded as videos (visualization 1, visualization 2) and are available online at stacks.iop.org/MST/28/075010/mmedia.

To better understand the vibrational state of the earphone diaphragm, we measured three different sub-areas of the diaphragm, namely area A, area B and area C, as marked in the red, green and blue rectangles, respectively, in figure 14(a). The vibrational frequency was controlled at 5 Hz. The vibration curves of three points marked in figure 14(a) are presented in figure 14(b). The amplitudes of these waveforms are not exactly the same. The green one has the largest amplitude because the green point just locates above the vibrator coil from where the waveform is delivered. Figures 14(c)–(e) are three height maps of three moments (80 ms, 130 ms and 180 ms) corresponding to the red marked area A in figure 14(a). The principal feature of this part is a spherical structure that can be clearly recognized. Figures 14(f)–(h) are three height maps of three moments (60 ms, 110 ms and 160 ms) corresponding to the green marked area B in figure 14(a). The gap structure is well reconstructed, which can be easily figured out from the changing color. Figures 14(i)–(k) are three height maps of three moments (150 ms, 200 ms and 250 ms) corresponding to the blue marked area C in figure 14(a). The small gaps in this area can be easily distinguished. A video corresponding to the three vibrations can be downloaded from the supplementary material for observation (visualization 3).

To test the system's performance for measuring a faster vibration of the earphone, we gradually increased the frequency of the driving signal to 10 Hz, 16 Hz and 20 Hz. The same area as shown in figure 14(c) is reconstructed. Figure 15 gives the results of the diaphragm vibrating at different frequencies. The related video is offered as supplementary material (visualization 4). Figures 15(a)–(c) are the 3D maps corresponding to three moments marked in figures 15(d)–(f). Figures 15(d)–(f) are the vibration curves of the red point marked in figure 14(a) at 10 Hz, 16 Hz and 20 Hz, respectively. The difference between figure 15(a) (10 Hz) and figure 14(d) (5 Hz) is not evident because neither of the two vibrational frequencies is big enough. However, when the vibrational frequency increases to 16 Hz, the measurement accuracy becomes worse, as shown in figure 15(b). This is because, as the images are captured, the points being measured shift to different positions. When the vibrational frequency increases to 20 Hz, the overall shape

of the diaphragm has become different from that expected. However, the overall sphere shape of the diaphragm and the sinusoidal vibration curve are still measurable, which indicates the robustness of our system.

5. Conclusions and future works

In this work, a microscopic 3D dynamic measurement technique is proposed. We effectively combine a binary structured pattern with a number–theoretical phase unwrapping algorithm to realize real-time microscopic 3D shape measurement. Based on the frequency-shifting principle of the SPWM technique, we present a strategy to generate optimized SPWM patterns with frequency components suitable for the property of the four-step phase-shifting algorithm. A DMD-based projector is used to achieve high speed and accurate projection of binary phase-shifting patterns. Only a slight defocusing level of the projected pattern suppresses almost high-order harmonics. With the help of the number–theoretical phase unwrapping method, the ambiguity of the phase orders can be successfully eliminated. Real-time 3D measurement is realized with the development of a fast data processing programme. The display rate can reach 120 FPS with a projection speed of 400 FPS. The experimental results reveal that our system can successfully realize microscopic 3D dynamic measurement with a good robustness with a measurement range of about 8 mm × 6 mm in lateral and 8 mm in depth.

Acknowledgments

References

[1] Gorthi S S and Rastogi P 2010 Fringe projection techniques: whither we are? *Opt. Lasers Eng.* **48** 133–40
[2] Zhang Q and Su X 2005 High-speed optical measurement for the drumhead vibration *Opt. Express* **13** 3110–6
[3] Zhang S 2010 Recent progresses on real-time 3D shape measurement using digital fringe projection techniques *Opt. Lasers Eng.* **48** 149–58
[4] Zuo C, Chen Q, Gu G, Feng S and Feng F 2012 High-speed three-dimensional profilometry for multiple objects with complex shapes *Opt. Express* **20** 19493–510
[5] Zhao H, Liang X, Diao X and Jiang H 2014 Rapid *in situ* 3D measurement of shiny object based on fast and high

[6] Feng S, Chen Q, Zuo C, Sun J and Yu S L 2014 High-speed real-time 3-d coordinates measurement based on fringe projection profilometry considering camera lens distortion *Opt. Commun.* **329** 44–56
[7] Windecker R, Fleischer M and Tiziani H J 1997 Three-dimensional topometry with stereo microscopes *Opt. Eng.* **36** 3372–7
[8] Proll K-P, Nivet J-M, Voland C and Tiziani H J 2000 Application of a liquid-crystal spatial light modulator for brightness adaptation in microscopic topometry *Appl. Opt.* **39** 6430–5
[9] Windecker R, Fleischer M, Krner K and Tiziani H J 2001 Testing micro devices with fringe projection and white-light interferometry *Opt. Lasers Eng.* **36** 141–54
[10] Zhang C, Huang P S and Chiang F-P 2002 Microscopic phase-shifting profilometry based on digital micromirror device technology *Appl. Opt.* **41** 5896–904
[11] Vargas J, Koninckx T, Quiroga J A and Van Gool L 2008 Three-dimensional measurement of microchips using structured light techniques *Opt. Eng.* **47** 053602–2
[12] Van der S, Soons J A M and Dirckx J J 2015 Real-time microscopic phase-shifting profilometry *Appl. Opt.* **54** 4953–9
[13] Li B and Zhang S 2016 Microscopic structured light 3D profilometry: binary defocusing technique versus sinusoidal fringe projection *Opt. Lasers Eng.* **96** 117–23
[14] Lei S and Zhang S 2009 Flexible 3-d shape measurement using projector defocusing *Opt. Lett.* **34** 3080–2
[15] Su X Y, Zhou W S, Von Bally G and Vukicevic D 1992 Automated phase-measuring profilometry using defocused projection of a Ronchi grating *Opt. Commun.* **94** 561–73
[16] Ayubi G A, Ayubi J A, Martino J M D and Ferrari J A 2010 Pulse-width modulation in defocused three-dimensional fringe projection *Opt. Lett.* **35** 3682–4
[17] Wang Y and Zhang S 2011 Superfast multifrequency phase-shifting technique with optimal pulse width modulation *Opt. Express* **19** 5149–55
[18] Wang Y and Zhang S 2012 Comparison of the squared binary, sinusoidal pulse width modulation, and optimal pulse width modulation methods for three-dimensional shape measurement with projector defocusing *Appl. Opt.* **51** 861–72
[19] Zuo C, Chen Q, Feng S, Feng F, Gu G and Sui X 2012 Optimized pulse width modulation pattern strategy for three-dimensional profilometry with projector defocusing *Appl. Opt.* **51** 4477–90
[20] Surrel Y 1996 Design of algorithms for phase measurements by the use of phase stepping *Appl. Opt.* **35** 51–60
[21] Zhong J and Zhang Y 2001 Absolute phase-measurement technique based on number theory in multifrequency grating projection profilometry *Appl. Opt.* **40** 492–500
[22] Hu Y, Chen Q, Tao T, Li H and Zuo C 2017 Absolute three-dimensional micro surface profile measurement based on a Greenough-type stereomicroscope *Meas. Sci. Technol.* **28** 045004
[23] Malacara D 2006 *Optical Shop Testing* 3rd edn (New York: Wiley)
[24] Zuo C, Chen Q, Gu G, Feng S, Feng F, Li R and Shen G 2013 High-speed three-dimensional shape measurement for dynamic scenes using bi-frequency tripolar pulse-width-modulation fringe projection *Opt. Lasers Eng.* **51** 953–60
[25] Zuo C, Huang L, Zhang M, Chen Q and Asundi A 2016 Temporal phase unwrapping algorithms for fringe projection profilometry: a comparative review *Opt. Lasers Eng.* **85** 84–103